NEUROPHYSIOLOGY

Tb^{3+}-doped fluorescent glass for biology

Kazuki Okamoto[1,2], Teppei Ebina[3], Naoki Fujii[4], Kuniaki Konishi[5], Yu Sato[1], Tetsuhiko Kashima[1], Risako Nakano[1], Hiroyuki Hioki[2], Haruki Takeuchi[1], Junji Yumoto[5,6], Masanori Matsuzaki[3], Yuji Ikegaya[1,7,8]*

Optical investigation and manipulation constitute the core of biological experiments. Here, we introduce a new borosilicate glass material that contains the rare-earth ion terbium(III) (Tb^{3+}), which emits green fluorescence upon blue light excitation, similar to green fluorescent protein (GFP), and thus is widely compatible with conventional biological research environments. Micropipettes made of Tb^{3+}-doped glass allowed us to target GFP-labeled cells for single-cell electroporation, single-cell transcriptome analysis (Patch-seq), and patch-clamp recording under real-time fluorescence microscopic control. The glass also exhibited potent third harmonic generation upon infrared laser excitation and was usable for online optical targeting of fluorescently labeled neurons in the in vivo neocortex. Thus, Tb^{3+}-doped glass simplifies many procedures in biological experiments.

INTRODUCTION

The optical observation and manipulation of cells in living tissues are widespread in current biological research and have revealed diverse biological properties in cells and intercellular communications. In particular, the real-time optical targeting of specific types of cells benefits single-cell electroporation, single-cell transcriptome profiling, and whole-cell recording because recent technical advances in genetic labeling have enabled the online identification of cells expressing fluorescent proteins (*1*, *2*), but it remains difficult to access fluorescently labeled cells using glass pipettes because the glass is not fluorescent in the visible light range. To visualize glass pipettes, some studies load fluorescent dyes inside the pipettes (*3*, *4*). However, the dyes ejected from the pipette tips often mask fluorescently labeled cells. This problem is especially severe in patch-clamp recordings because positive pressure is continuously applied through the pipettes during cell targeting. Other studies coat the surface of pipette tips with chemical fluorophores (*5*, *6*), quantum dots (*7*–*9*), or fluorescent silica nanoparticles (*10*). To date, these techniques have not become popular, probably because the dyes on the tip surfaces make it difficult to form seals with the plasma membrane of target cells (*11*) and because the dye-coating procedure adds a laborious step and increases the risk of breaking or soiling the glass tips. Moreover, coated dyes are often subject to rapid photobleaching; otherwise, they would be costly.

To solve these problems, we introduce a new composition of borosilicate glass. Rare-earth ions display unique fluorescence emissions that have sharp peaks in the visible light spectrum. The emissions are independent of the environment (*12*–*14*) and are often stable even in glass (*15*–*17*). Among rare-earth ions, we focused on terbium(III) (Tb^{3+}). Tb^{3+} has complex energy level structures (Fig. 1A), among which the $^7F_6 \rightarrow {}^5D_4 \rightarrow {}^7F_5$ radiative transition is theoretically expected to emit green fluorescence at a wavelength of 543 nm upon excitation at a peak wavelength of 484 nm (*14*, *18*). This excitation wavelength is near the highest visibility for human eyes (*19*, *20*) and is also close to that of green fluorescent protein (GFP), which has a peak excitation at 475 nm. Thus, pipettes made of Tb^{3+}-doped glass are versatile for fluorescence-targeted single-cell manipulations, including electroporation, transcriptome analysis, and patch-clamp recording.

[1]Graduate School of Pharmaceutical Sciences, The University of Tokyo, Tokyo, Japan. [2]Department of Cell Biology and Neuroscience, Juntendo University Graduate School of Medicine, Tokyo, Japan. [3]Department of Physiology, Graduate School of Medicine, The University of Tokyo, Tokyo, Japan. [4]AGC Inc., Tokyo, Japan. [5]Institute for Photon Science and Technology, The University of Tokyo, Tokyo, Japan. [6]Department of Physics, The University of Tokyo, Tokyo, Japan. [7]Institute for AI and Beyond, The University of Tokyo, Tokyo, Japan. [8]Center for Information and Neural Networks, National Institute of Information and Communications Technology, Suita City, Osaka, Japan.
*Corresponding author. Email: yuji@ikegaya.jp

RESULTS

Tb^{3+}-doped glass pipettes

We created borosilicate glass containing 3.1 mole percent (mol %) Tb_2O_3. The Tb^{3+}-doped glass emitted green fluorescence, which was visible to the naked human eye even under room light (fig. S1). We investigated its transmission spectrum for wavelengths ranging from 200 to 2700 nm (fig. S2A). Tb^{3+}-doped glass had an absorption peak at a wavelength of 484 nm, which was not observed in normal borosilicate glass without Tb^{3+} (fig. S2B). Because of the popularization of GFP in biology, argon-ion lasers and diode lasers emitting 488 nm are widely used in various experiments, such as fluorescence observation, optogenetic stimulation, and flow cytometry. Upon 488-nm excitation, Tb^{3+}-doped glass exhibited green fluorescence with a peak wavelength of 542 nm (Fig. 1B). The quantum yield of Tb^{3+}-doped glass at 488-nm excitation was as high as 68.4%. Similar to the control borosilicate glass, Tb^{3+}-doped glass was physically stable without crystallization or phase separation even at a high temperature of 750°C for at least 60 min. Grains of the glass had a high hydrolytic resistance at 121°C (table S1). The coefficient of thermal expansion of the glass was 7.5×10^{-6} K^{-1}, which was also similar to that of the control glass (fig. S3). These features provide Tb^{3+}-doped glass with plasticity suitable for free molding without loss of fluorescence.

We succeeded in producing glass capillaries (Fig. 1C) and pipettes using conventional micropipette pullers. The molded glass still emitted green fluorescence, and the pipette tips were visible to the eyes using conventional epifluorescence microscopes with xenon or xenon-mercury lamps (Fig. 1D). Scanning electron microscopic inspection did not reveal any aberration of the pipette tips that might affect the quality of electrophysiological recording (Fig. 1E). The pipette resistance did not differ between the control and Tb^{3+}-doped glass ($P = 0.62$, $t_{94} = 0.49$, $n = 48$ pipettes, Student's t test; Fig. 1F). The capacitance of Tb^{3+}-doped pipettes was slightly higher than that of pipettes without Tb^{3+} ($P = 8.6 \times 10^{-13}$, $t_{13} = 26.9$, $n = 7$

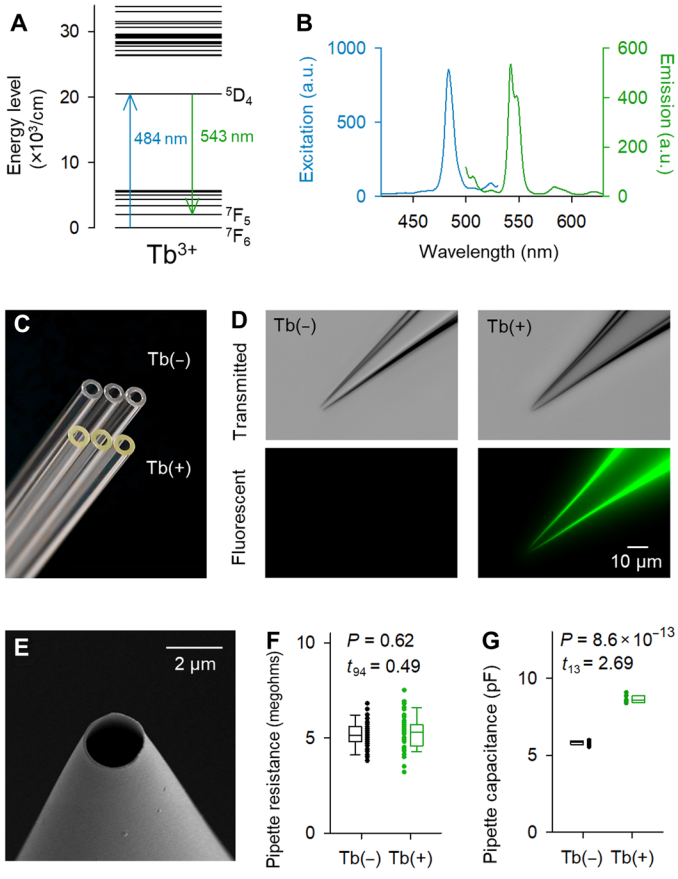

Fig. 1. Tb^{3+}-doped pipettes emit green fluorescence. (**A**) Partial energy level diagram of Tb^{3+} [extracted partially from (*14*)]. (**B**) Excitation (blue) and emission (green) spectra of 3.1 mol % Tb^{3+}-doped glass. (**C**) Macroscopic color photograph of control (top) and Tb^{3+}-doped (bottom) glass capillaries. Photo credit: Yuji Ikegaya, The University of Tokyo. (**D**) Bright-field monochromatic (top) and fluorescence (bottom) images of the tips of control (left) and Tb^{3+}-doped (right) glass pipettes (488-nm laser excitation at 25 mW). Pipettes made of Tb^{3+}-doped glass emitted green fluorescence. Photo credit: Kazuki Okamoto, The University of Tokyo and Juntendo University. (**E**) Scanning electron microscopy image of the tip of a Tb^{3+}-doped pipette. Photo credit: Hiroyuki Hioki, Juntendo University. (**F**) Pipette resistances of control (black) and Tb^{3+}-doped pipettes (green). The rectangles show the medians and the 25th and 75th percentiles, and the whiskers display the 10th and 90th percentiles. $n = 48$ pipettes, Student's t test. (**G**) The same as (F) but for pipette capacitances. $n = 7$ to 8 pipettes, Student's t test.

and 8 pipettes, Student's t test; Fig. 1G); however, this capacitance was still acceptable for whole-cell patch-clamp recording and did not reduce the recording quality (see below). We found no evidence of photobleaching of Tb^{3+}-doped pipettes even under continuous xenon-lamp illumination, in contrast to previously reported dye-coated pipettes [$P = 1.1 \times 10^{-7}$, $F_{1,32} = 46$, $n = 5$ pipettes, two-way analysis of variance (ANOVA); fig. S4].

Single-cell gene electroporation using Tb^{3+}-doped pipettes

Using Tb^{3+}-doped micropipettes, we first conducted the single-cell electroporation of tdTomato, a red fluorescent protein, into neurons in rat organotypic hippocampal slice cultures. A Tb^{3+}-doped pipette containing a pCMV-tdTomato vector and CA1 pyramidal cells that were sparsely labeled with enhanced GFP (EGFP) were simultaneously

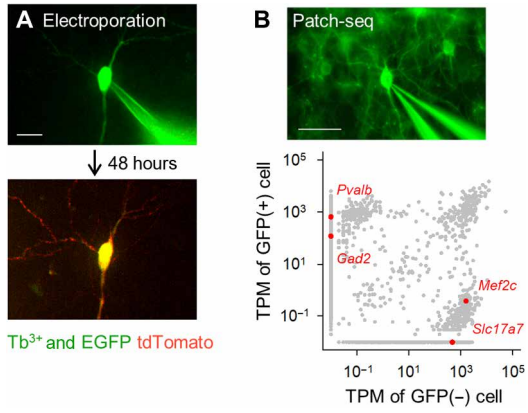

Fig. 2. Fluorescently targeted single-cell electroporation and transcriptome analysis using Tb^{3+}-doped pipettes. (**A**) Single-cell gene electroporation using Tb^{3+}-doped pipettes. A Tb^{3+}-doped pipette containing a pCMV-tdTomato vector was attached to an EGFP-positive hippocampal pyramidal cell in an organotypic culture (top; DiV 16), and electrical pulses were applied. After 48 hours, the targeted neuron expressed tdTomato (bottom). Scale bar, 20 µm. (**B**) Patch-seq using Tb^{3+}-doped pipettes. A Tb^{3+}-doped pipette was attached to a GFP-positive GABAergic interneuron in a cortical acute slice of a PV-GFP transgenic mouse, and RNA was extracted by applying suction (top). Scale bar, 50 µm. Transcripts per million (TPM) of GFP-positive and GFP-negative cells (bottom). Gray dots indicate all detected gene transcripts. Red dots are representative unique gene transcripts, *Pvalb* and *Gad2* (GAD65) for GFP-positive cell versus *Mef2c* and *Slc17a7* (VGLUT1) for non–GFP-positive cell. Photo credit: Kazuki Okamoto, The University of Tokyo and Juntendo University.

visualized under an epifluorescence microscope (Fig. 2A, top). An EGFP-positive cell was selected and approached using a Tb^{3+}-doped pipette; note that we did not need to switch the light path during the approach, because the pipettes and EGFP have similar fluorescence characteristics and can be visualized using the same optical apparatus. The pipette tips were physically attached to the cells, and electrical pulses were applied for electroporation. After 48 hours, the targeted neurons expressed tdTomato (Fig. 2A, bottom).

Single-cell RNA sequencing using Tb^{3+}-doped pipettes

We next performed quantitative single-cell RNA sequencing (Patch-seq) (*21*–*23*) from parvalbumin (PV)–positive GABAergic neurons in acute slices of the mouse primary motor cortex of PV-GFP transgenic mice (*24*). A PV-GFP–positive cell was patch-clamped by optical targeting with a Tb^{3+}-doped pipette (Fig. 2B, top), and RNA was extracted by negative pressure. We also extracted RNA from a neighboring PV-GFP–negative cell, a putative pyramidal cell. When the collected RNA was sequenced, 14 million reads (25%) and 22 million reads (42%) were uniquely mapped for PV-GFP–positive and PV-GFP–negative cells, respectively (Fig. 2B, bottom).

In vitro patch-clamp recordings using Tb^{3+}-doped pipettes

We conducted patch-clamp recordings from primary cultures of hippocampal neurons that were sparsely labeled with EGFP using a Tb^{3+}-doped pipette loaded with red fluorescent Alexa Fluor 594 (Fig. 3A). The targeted cells were filled with Alexa Fluor 594 when successfully held by the pipette in the whole-cell configuration. The same method was also applicable to acute brain slice preparations (Fig. 3B), in which neurons are located deeper in less transparent tissues than cultured neurons. We patched CA1 pyramidal cells in acute hippocampal slices using Tb^{3+}-doped pipettes. These neurons

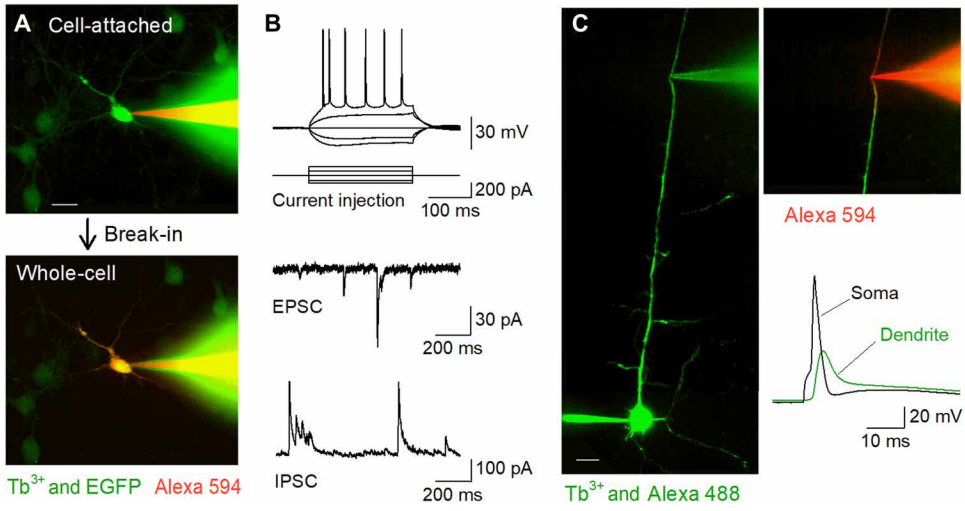

Fig. 3. Fluorescently targeted patch-clamp recordings in vitro using Tb^{3+}-doped pipettes. (**A**) Nipkow-disk confocal images during patch-clamp recording from an EGFP-positive cultured hippocampal neuron (green) using a Tb^{3+}-doped pipette (green) filled with Alexa Fluor 594 (red). The cell was trapped in the cell-attached mode (top) and then held in the whole-cell mode (bottom). Scale bar, 20 μm. (**B**) Representative waveforms of action potentials induced by current injection (top), spontaneous EPSCs (middle), and spontaneous IPSCs (bottom) recorded from CA1 pyramidal cells in acute hippocampal slices using Tb^{3+}-doped pipettes. (**C**) Targeted dendritic patch-clamp recordings using Tb^{3+}-doped pipettes. A layer 5 pyramidal cell was loaded intracellularly with Alexa Fluor 488 via somatic whole-cell recording, and its apical dendrite was targeted for further whole-cell recording using a Tb^{3+}-doped pipette under Nipkow-disk confocal visualization. Scale bar, 20 μm. After break-in, the dendrite was visualized by Alexa Fluor 594 loaded intracellularly via the Tb^{3+}-doped pipette (right top). A backpropagating action potential was recorded by the Tb^{3+}-doped pipette following an action potential evoked in the soma (right bottom). Photo credit: Kazuki Okamoto, The University of Tokyo and Juntendo University.

exhibited normal action potentials in response to brief current injection under the current-clamp configuration. They also exhibited normal spontaneous excitatory and inhibitory postsynaptic currents (EPSCs and IPSCs) under the voltage-clamp configuration. To examine the noise level in the signal recorded using Tb^{3+}-doped pipettes, we monitored miniature EPSCs in the presence of 1 μM tetrodotoxin (fig. S5A). Neither the sizes nor the frequencies of the miniature EPSPs differed between Tb^{3+}-doped pipettes and conventional pipettes without Tb^{3+} (fig. S5, B and C), nor did their signal-to-noise ratio differ (fig. S5D). Tb^{3+}-doped pipettes were used for long-term stable recordings; neither the waveforms (fig. S6A) nor the amplitudes of evoked EPSCs changed for 60 min ($P = 0.34$, $J = 0.41$, $n = 4$ cells, Jonckheere-Terpstra trend test; fig. S6B). Tb^{3+}-doped pipettes were also useful for recordings from neurites (Fig. 3C). After neurons were intracellularly loaded with Alexa Fluor 488 via somatic whole-cell patch-clamp pipettes, dendrites visualized with green fluorescence were targeted using Tb^{3+}-doped pipettes at 488-nm excitation under a spinning-disk confocal microscope. Upon somatic activation, backpropagating action potentials were recorded from the targeted dendrites (Fig. 3C).

In vivo patch-clamp recordings using Tb^{3+}-doped pipettes

We next characterized the nonlinear multiphoton excitation of Tb^{3+}-doped glass (Fig. 4A). We illuminated the glass with infrared light at wavelengths that were approximately double the single-photon excitation peak (484 nm) of Tb^{3+}. The Tb^{3+}-doped pipettes emitted green fluorescence that was captured using a photomultiplier tube through a 495- to 540-nm band-pass filter. The 495- to 540-nm emission peaked at an excitation wavelength of 975 nm (Fig. 4B), which suggests that the 975-nm laser excited Tb^{3+}-doped glass through a two-photon absorption process. However, unexpectedly, we could not observe the shapes of the pipette tips (Fig. 4A, middle). This was due to the raster scanning microscopy and the long lifetime of the green fluorescence of Tb^{3+}-doped glass ($\tau_{1/2} = 2.8$ ms; Fig. 4B, inset). The signal at a pixel, which is detected by the GaAsP photomultiplier tube, corresponds to the focal point of two-photon excitation. However, the laser scanning speed in two-photon microscopy when cells are observed is typically several microseconds per pixel, and the afterglow of the Tb^{3+} green light led to artifactual signal in pixels where the Tb^{3+}-doped pipette did not exist when the specimens were raster-scanned.

On the other hand, another bright signal at 1300-nm excitation (Fig. 4A, bottom) was observed through a 410- to 450-nm band-pass filter (Fig. 4C). Spectrometric inspections revealed that the emission intensity peaked at a wavelength of 431 nm, which corresponds to nearly one-third of the 1300-nm excitation wavelength (Fig. 4D). Given that the energy levels in Tb^{3+} are not compatible with two-photon or three-photon excitation by a 1300-nm excitation wavelength (Fig. 1A), the signal likely arose from third harmonic generation (THG). Consistent with this idea, the emission intensity approximated a cubic curve as a function of the excitation intensity (scaling exponent = 3.0, y intercept = $10^{-2.9}$; Fig. 4E). The THG had little afterglow, and the pipette tips were visualized by raster scanning (Fig. 4A, bottom). THG is also intrinsic in normal Tb^{3+}-free glass, but the THG of Tb^{3+}-doped glass was stronger than that of control borosilicate glass without Tb^{3+} [Tb(−): 2.9 ± 0.3 arbitrary units (a.u.), Tb(+): 9.4 ± 2.5 a.u., $P = 3.8 \times 10^{-4}$, $t_8 = 5.9$, $n = 5$ pipettes, Student's t test; Fig. 4, F and G]. By taking advantage of the strong THG signal of Tb^{3+}-doped pipettes, we conducted in vivo whole-cell patch-clamp recordings using a multiphoton laser microscope. Layer 2/3 pyramidal cells in the primary motor cortex that had been transfected with adeno-associated virus carrying the tdTomato gene were optically targeted. The cells and Tb^{3+}-doped pipette were simultaneously visualized using dual-laser irradiation at 1040 and 1300 nm, respectively

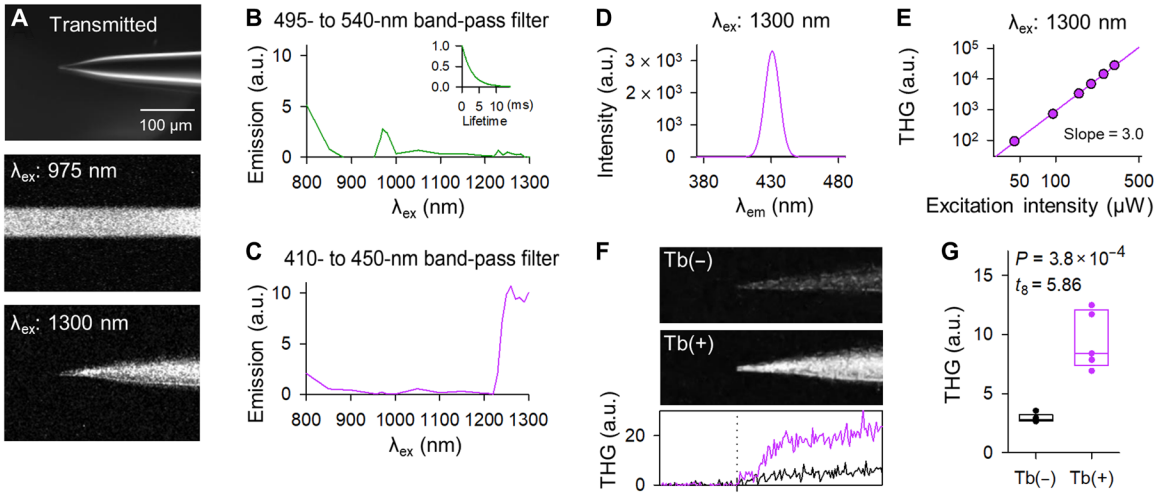

Fig. 4. Tb^{3+}-doped pipettes emit THG upon 1300-nm laser excitation. (**A**) Representative images of the tip of a Tb^{3+}-doped pipette in the bright field (top), two-photon fluorescence upon 975-nm laser excitation (middle), and three-photon harmonic emission upon 1300-nm laser excitation (bottom). The middle and bottom images were acquired with a horizontal scanning of 2 μs per pixel and *z*-stacked. (**B**) The excitation spectrum through a 495- to 540-nm band-pass filter. The inset graph indicates the fluorescence decay curve upon 975-nm excitation. (**C**) The same as (B) but through a 410- to 450-nm band-pass filter. (**D**) The emission spectrum upon 1300-nm excitation was measured using a monochromator. (**E**) Double logarithmic plot of the THG intensity as a function of the 1300-nm laser power. The regression line had a slope of 3.0. (**F**) THG images of the tips of the control (top) and Tb^{3+}-doped pipettes (middle). The images were *z*-stacked. The bottom graph depicts the THG intensity of control (black) and Tb^{3+}-doped pipettes (purple). The vertical dotted line indicates the tip location. (**G**) The THG intensities of Tb^{3+}-doped pipettes (purple) were stronger than those of control pipettes (black). The rectangles show the medians and the 25th and 75th percentiles. $n = 5$ pipettes, Student's *t* test. Photo credit: Teppei Ebina, The University of Tokyo.

(Fig. 5A). Current injection-induced action potentials (Fig. 5B) and spontaneous membrane fluctuations (Fig. 5C) were recorded under the current-clamp configuration.

DISCUSSION

We invented Tb^{3+}-doped glass that emitted green fluorescence strong enough to be recognized by the naked human eye. The glass had similar physical properties to conventional borosilicate glass (except for the fluorescence) and did not exhibit apparent photobleaching or cytotoxicity. Thus, pipettes made of Tb^{3+}-doped glass enabled online fluorescence manipulations, including optical targeting of single-cell electroporation, single-cell RNA sequencing, and electrophysiological recordings. In addition, the glass emitted THG upon three-photon excitation and was applicable for in vivo manipulations. We thus believe that the single-photon green fluorescence and THG of Tb^{3+}-doped glass provide a platform applicable for multiple purposes in biological research.

Glass pipettes are an irreplaceable material for patch-clamp recordings (*25*). The composition of the glass has changed little in the past 30 years because the composition of the glass has a notable impact on pipette formation and recording quality (*26*, *27*). Thus, glass pipettes for the patch-clamp technique were not developed, despite significant advances in biological technology. Rather, glass materials have been independently developed in the engineering field. Rare-earth ion doping is a useful technology for optics. Tb^{3+}-doped glass has also been invented for optical purposes to manipulate visible lasers (*16*). In this work, we proposed a new application of fluorescent glass and improved the targeted patch-clamp technique.

The method of patch clamping has undergone many innovations and developments, including planar patch clamping (*28*, *29*), pipette cleaning (*30*), and automated patch clamping (*31*–*33*). However, "targeted" patch clamping is still difficult to automate, mainly because it requires an automatic image recognition system, in which the tip of the pipette provides a clue as to its location (*34*, *35*). In this respect, Tb^{3+}-doped pipettes may support automation and human experimenters.

The emissions of rare-earth ions derive from the activity of 4f electrons, which are shielded by the $5s^2 5p^6$-closed shells and are independent of other orbitals. Thus, their fluorescence is stable and is minimally affected by their ligands and environments. Probably because of this stability, Tb^{3+}-doped glass displayed similar excitation and emission to Tb^{3+} solution and other Tb^{3+} compounds. We observed two-photon excitation of Tb^{3+}-doped glass, but the long lifetime of its emission may limit its biological application (Fig. 4B, inset). The f-f transition of rare-earth elements is prohibitive and requires intersystem crossing, which may extend the fluorescence lifetime of rare-earth ions (*36*). Thus, we could not observe the tips of fluorescent pipettes under 975-nm excitation using raster scanning two-photon microscopy (Fig. 4A, middle). The lifetime of emission varies with the codoping of another rare-earth ion, but it is difficult to maintain the emission wavelength of 543 nm. The lifetime may also be reduced at concentrations of more than 4 mol % Tb^{3+}, but such higher Tb^{3+} concentrations destabilize glass (*16*). The reduction in lifetime is thought to be on the order of milliseconds and is still insufficient to enable raster scanning in two-photon microscopy.

However, the THG of Tb^{3+} is short-lived enough to be applicable to photomultiplier-based raster scanning imaging. THG is one of the nonlinear optic phenomena that occur at high densities of photons. Among rare-earth ions, Gd^{3+} and Yb^{3+} have been used as ingredients in nonlinear optical crystals (*37*, *38*), but few studies have characterized the nonlinear optics of Tb^{3+}-doped materials. As pulse lasers at 800 nm are reported to induce the three-photon excitation and fluorescence of Tb^{3+} (*39*, *40*), we observed the fluorescence of Tb^{3+}-doped pipettes upon excitation at 800 nm (Fig. 4B); at

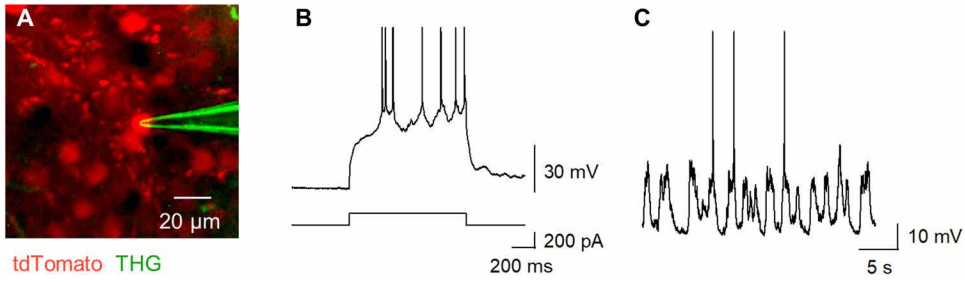

Fig. 5. THG-based in vivo patch-clamp recordings using Tb^{3+}-doped pipettes. (**A**) Multiphoton image of an in vivo patch-clamp recording guided by THG of Tb^{3+}-doped pipettes, targeting a cell labeled with tdTomato, which underwent two-photon excitation by a 1040-nm laser (red). The THG of the Tb^{3+}-doped pipette was obtained using a 1300-nm laser (green). (**B**) Action potentials evoked by a step current injection (bottom) into a layer 2/3 pyramidal cell in the primary motor cortex (top) of an anesthetized mouse were recorded using a Tb^{3+}-doped pipette. (**C**) Spontaneous membrane potentials were recorded using a Tb^{3+}-doped pipette. Photo credit: Teppei Ebina, The University of Tokyo.

this wavelength, however, the emission was so weak that we could not observe the tips of the pipettes.

Even without Tb^{3+}, normal borosilicate glass exhibits THG, but its intensity is insufficient for targeted patch-clamp recordings because some biological structures, such as the myelin sheath and blood vessels, emit intrinsic THG at 1300-nm excitation (*41*, *42*) and cause background noise. Tb^{3+} strengthened the THG of glass to a level suitable for practical use; note that 1300 nm is a zero-dispersion wavelength in glass, which enhances the cubic nonlinear optical effects (Fig. 4, F and G) (*43*, *44*). We observed a strong THG signal in vivo in the neocortical layer 2/3 parenchyma against background THG noise. Near-infrared light of 1300 nm can reach deep brain tissue with little absorption by hemoglobin (*45*, *46*). For example, the three-photon imaging of hippocampal neurons is implemented with 1300-nm excitation (*41*). However, under our conditions, the THG wavelength of Tb^{3+} was 431 nm and was susceptible to absorption and diffusion in brain tissues. The problem will be solved with longer-wavelength excitation. Laser wavelengths over 1300 nm have not yet prevailed for multiphoton microscopy, but a 1700-nm laser is already used to observe deep brain tissue (*42*). Therefore, we expect technical advances in infrared lasers to expand the application of Tb^{3+}-doped pipettes.

Last, other rare-earth ion doping could also be useful for biological experiments. For instance, Eu^{3+}- and Eu^{2+}-doped glass emit red and blue fluorescence, respectively (*47*, *48*). Therefore, fluorescent pipettes are available at different wavelengths. In addition to patch-clamp pipettes, rare-earth ion-doped glass can be molded into any shape. For example, glass fibers and nanoparticles made of Tb^{3+}-doped glass may irradiate a broad area of a deep brain region and may be usable as an optogenetics tool. We believe that the fluorescence emitted by Tb^{3+}-doped and other rare-earth ion-doped glass can be exploited by new ideas to open new frontiers in biological research.

METHODS

Tb^{3+}-doped glass capillaries

Tb^{3+}-doped glass consisted of 62.6 mol % SiO_2, 4.9 mol % Al_2O_3, 9.8 mol % B_2O_3, 14.0 mol % Na_2O, 5.5 mol % MgO, 3.1 mol % Tb_2O_3, and 0.1 mol % CeO_2. The starting materials were 99.9% pure SiO_2, Al_2O_3, B_2O_3, Na_2CO_3, MgO, Tb_4O_7, and CeO_2. Approximately 300-g batches of the materials were fully melted within a platinum crucible in an electronic furnace at 1500°C. For the first 1 hour, the glass melt was stirred at 1500°C. Then, the melt was poured onto a steel plate, annealed at 630°C for 1 hour, and gradually cooled at a rate of 0.5°C/min in an electric furnace. The glass block was cut into a cylindrical shape (outer diameter: 9.0 mm, inner diameter: 5.1 mm, and length: 100 mm). This tube-shaped glass was pulled at 550° to 650°C to obtain glass capillaries (outer diameter: 1.5 mm, inner diameter: 0.85 mm, and length: 100 mm). The source of Tb^{3+} was Tb_4O_7, which contained Tb^{3+} and Tb^{4+}. By the addition of CeO_2 in batches, we improved the quantum yield of Tb^{3+}-doped glass from 48.8 to 68.4%. The final Tb^{3+} concentration in the glass was 3.1 mol %, which corresponded to 1.5×10^{21} ions/cm^3.

Terbium-doped glass properties

The excitation and emission spectra were measured through a 0.69-mm-thick glass plate using an F-4500 spectrofluorometer (Hitachi High-Technologies). The transmittance spectra were measured through 1.00-mm-thick glass plates using an ultraviolet-visible/NIR spectrophotometer (V-770, JASCO). The quantum yield was measured in a glass block (10 cm by 10 cm by 10 cm) using Quantaurus-QY (Hamamatsu Photonics). To obtain the image shown in Fig. 1D, the tips of the pipettes were coated with osmium with an osmium plasma coater (OPC80T, Filgen) and observed with a scanning electron microscope (S-4800, Hitachi High-Technologies). Thermomechanical analysis (TMA; TD-5000SA, Bruker) was performed on glass rod samples measured at a heating rate of 5°C/min from room temperature to 680°C. The coefficient of thermal expansion was calculated on the linear section of the curve (range from 50° to 350°C). The glass transition temperature was determined as a change in the slope of the curve. The sag temperature (glass viscosity: approximately 10^{10} dPa·s) was determined by TMA as the point at which the glass rod started to sag (loading weight: 5 g). The dielectric constant was measured with 0.7 mm thickness using a Precision LCR meter (E4980A, Agilent) and the dielectric test fixture (16541B, Agilent). The Tb^{3+}-doped pipettes were pulled using a P-1000 micropipette puller (Sutter Instrument). The pipette capacitance was measured on the surface of a Sylgard bead (*49*).

Animal experiment ethics

Experiments were performed with the approval of the Animal Experiment Ethics Committee at the University of Tokyo (approval no. P29-3, P29-9) and according to the University of Tokyo guidelines for the care and use of laboratory animals.

Primary culture preparation

Primary cultures were used for in vitro patch-clamp recordings. Dissociated hippocampal cells were prepared from postnatal 0-day-old C57BL/6J mice (*50*). The hippocampi were dissociated in pre-warmed Hanks' balanced salt solution and treated with 0.25% trypsin/EDTA at 37°C for 15 min. Next, the tissue was treated with 0.01% deoxyribonuclease I (Sigma-Aldrich) at room temperature for 5 min and washed with Hanks' balanced salt solution, which was then replaced with Neurobasal plating medium containing 2% B27 supplement, 0.5 mM glutamine, 25 μM glutamate, 0.1% penicillin, 0.1% streptomycin, 1 mM Hepes, and 10% horse serum. The tissues were triturated with Pasteur pipettes and filtered through a 40-μm-pore cell strainer (Corning). The dissociated cells were plated onto 13-mm coverslips coated with poly-D-lysine at a cell density of 8.0×10^4 cells per well in culture medium in 24-well plates and were incubated at 37°C in a humidified 5% CO_2 atmosphere. The medium was changed on day in vitro (DiV) 1 and thereafter every 3 days. The cells were treated with AAV-hSyn-EGFP [1.4×10^{12} vector genomes (vg)/ml] at DiV 7. Whole-cell recordings were performed on DiV 9.

Acute slice preparation

Acute slices were prepared from the hippocampi and cerebral cortices of ICR mice (17 to 28 postnatal days). The mice were anesthetized with isoflurane and decapitated. The brains were removed and placed in ice-cold oxygenated (95% O_2/5% CO_2) artificial cerebrospinal fluid (aCSF) containing 127 mM NaCl, 1.6 mM KCl, 1.24 mM KH_2PO_4, 1.3 mM $MgSO_4$, 2.4 mM $CaCl_2$, 26 mM $NaHCO_3$, and 10 mM glucose. The brains were sliced horizontally or coronally at a thickness of 400 μm using a vibratome (VT1200S, Leica) in ice-cold, oxygenated modified aCSF consisting of 222.1 mM sucrose, 27 mM $NaHCO_3$, 1.4 mM sodium phosphate buffer, 2.5 mM KCl, 1.0 mM $CaCl_2$, 7.0 mM $MgSO_4$, and 0.5 mM ascorbic acid, as previously described (*51*). Slices were maintained for 30 min at 35°C in oxygenated aCSF and then incubated for at least 30 min at room temperature before use.

In vitro electrophysiology

All recordings were performed at 33° to 35°C. Whole-cell recordings were obtained from hippocampal CA1 pyramidal cells or layer 5 pyramidal cells in the somatosensory cortex using a MultiClamp 700B amplifier and a Digidata 1550A digitizer controlled by pCLAMP10.5 software (Molecular Devices). Glass pipettes (3 to 6 megohms) were filled with a solution containing 130 mM CsMeSO$_4$, 10 mM CsCl, 10 mM Hepes, 10 mM Na_2-phosphocreatine, 4.0 mM MgATP, 0.3 mM Na_2GTP or 120 mM K-gluconate, 5.0 mM KCl, 1.0 mM $MgCl_2$, 10 mM Hepes, 0.2 mM EGTA, 10 mM Na_2-phosphocreatine, 2.0 mM MgATP, and 0.1 mM Na_2GTP.

Single-cell RNA sequencing

Glass pipettes (3 to 5 megohms) were filled with 1 μl of solution containing 120 mM K-gluconate, 5.0 mM KCl, 1.0 mM $MgCl_2$, 10 mM Hepes, 0.2 mM EGTA, 10 mM Na_2-phosphocreatine, 2.0 mM MgATP, and 0.1 mM Na_2GTP. While cells were held in the whole-cell voltage-clamp mode, a moderate negative pressure (approximately −50 mPa) was applied for 3 to 8 min. After the cytosol was obtained by this method, the intrapipette solution was pressure-ejected into 100 μl of lysis buffer (LB1 in NucleoSpin RNA Plus XS, Clontech), and total RNA was isolated with NucleoSpin RNA Plus XS (Clontech). Isolated total RNAs were converted to complementary DNA and amplified with the SMART-Seq v4 Ultra Low Input RNA Kit for Sequencing (Clontech). The final sequencing libraries were constructed with the Nextera XT DNA Library Prep Kit (Illumina) and the Nextera XT Index Kit (Illumina). The pooled sequencing library was analyzed on a NovaSeq 6000 (Illumina). Reads were aligned to the mouse genome (mm10 assembly; Ensembl Genome Browser) using STAR (v2.7.3a). Read counts were calculated using RSEM (v1.3.3).

Slice culture preparation and electroporation

Organotypic slice cultures were used for single-cell electroporation. Entorhinal-hippocampal organotypic slices were prepared from 7-day-old Wistar/ST rats as previously described (*52*, *53*). Rat pups were anesthetized by hypothermia and decapitated. The brains were removed and placed in ice-cold oxygenated Gey's balanced salt solution supplemented with 25 mM glucose. The tissues were sliced horizontally at a thickness of 300 μm using a vibratome (DTK-1500, Dosaka). The slices were placed on Omnipore membrane filters (JHWP02500, Millipore) and incubated in 5% CO_2 at 37°C. The culture medium—which was composed of 50% minimal essential medium, 25% Hanks' balanced salt solution, 25% horse serum, 0.1% penicillin, and 0.1% streptomycin—was changed every 3.5 days. Phosphate-buffered saline containing AAV-hSyn-EGFP (1.4×10^{11} vg/ml) was dripped onto the slices on DiV 1. Experiments were performed on DiV 12 to 19. For electroporation, pipettes were filled with intracellular solution including pCMV-tdTomato vector (100 ng/μl; gift from Koyama R.) and attached to target cells. Stimulation was 200 electric pulses with a duration of 1 ms and an amplitude of 0.4 V at 200 Hz (*54*).

Virus injection and surgical procedures in vivo

Postnatal 8-week-old mice (male, C57BL/6J) were anesthetized by an intramuscular injection of ketamine (74 mg/kg) before the surgery. After the mice were anesthetized, a 2 × 4 mm craniotomy was performed over the left forelimb primary motor cortex (approximately 0.2 mm anterior and 1.0 mm lateral to the bregma) as previously described (*55*). Before virus injection, a pulled glass pipette (broken and beveled to a 25- to 30-μm outer diameter; Sutter Instruments) and a 5-μl Hamilton syringe were back-filled with mineral oil (Nacalai Tesque) and front-loaded with virus solution. Layer 2/3 of the left forelimb primary motor cortex was stereotaxically targeted, and a total of 1 μl of AAV1-CaMKII-Cre (1.6×10^{11} vg/ml) and AAV1-CAG-Flex-tdTomato (4.8×10^{12} vg/ml) was injected at 0.02 μl/min using a syringe pump (KDS310). After injection, the pipette was maintained in place for 10 min and then slowly withdrawn. A 2-mm by 4-mm glass coverslip (#4 thickness; Matsunami Glass) was pressed onto the brain surface, and its edges were sealed with dental cement. One week after virus injection, the mice were anesthetized with 1% isoflurane and used for recording and imaging. Before the experiment, the glass window was replaced with 3% agarose (w/v). A 3-mm by 3-mm glass coverslip (#1 thickness; Matsunami Glass) was pressed onto the agarose surface, and its edges were sealed with a silicone elastomer (Kwik-Cast; World Precision Instruments).

Multiphoton imaging and in vivo electrophysiology

Multiphoton images were acquired with an FVMPE-RS system (Olympus), a 25× water immersion objective lens (XLPLN25XSVMP2, Olympus), and a broadly tunable laser with a pulse width of 120 fs and a repetition rate of 80 MHz (InSight DS+ Dual, Spectra Physics) as previously described (*56*). The signals passed through emission

filters of 410 to 455 nm or 495 to 540 nm (V30-FVG, Olympus) and were collected using a GaAsP photomultiplier tube (Hamamatsu Photonics). The frame acquisition rate was 1 frame/s, with two galvanometric scanning mirrors for the x and y axes. The pixel dwell time was 2 μs, and the size of the imaging fields was 512 × 512 pixels (0.994 μm per pixel for pipette imaging and 0.249 μm per pixel for in vivo imaging). To take pipette images, pipettes were filled with Milli-Q, and the images were z-stacked. For whole-cell recordings, pipettes were filled with intracellular solution containing 135 mM K-gluconate, 4.0 mM KCl, 10 mM Hepes, 0.3 mM EGTA, 10 mM Na_2-phosphocreatine, 4.0 mM MgATP, 0.3 mM Na_2GTP, and 0.2% biocytin.

THG measurement

The light source was a regeneratively amplified femtosecond laser (Astrella1K-USP, Coherent Inc.) and an optical parametric amplifier (HE-TOPAS-Prime-UV2, Light Conversion Ltd.) operating at a wavelength of 1300 nm with a pulse duration of 80 fs at a repetition rate of 1 kHz. Attenuated laser pulses with less than 0.5 mW average power through the ND filter were focused onto the sample glass with a diameter of approximately 30 μm. The THG signals collinear to the incident beam were analyzed by a monochromator (SR163, Andor Technology) with a charge-coupled device camera (DU420LC-BU2, Andor Technology). The measurement was performed at room temperature.

SUPPLEMENTARY MATERIALS

Supplementary material for this article is available at http://advances.sciencemag.org/cgi/content/full/7/2/eabd2529/DC1

View/request a protocol for this paper from *Bio-protocol*.

REFERENCES AND NOTES

1. J. Marshall, R. Molloy, G. W. Moss, J. R. Howe, T. E. Hughes, The jellyfish green fluorescent protein: A new tool for studying ion channel expression and function. *Neuron* **14**, 211–215 (1995).
2. M. Chalfie, Y. Tu, G. Euskirchen, W. W. Ward, D. C. Prasher, Green fluorescent protein as a marker for gene expression. *Science* **263**, 802–805 (1994).
3. K. Kitamura, B. Judkewitz, M. Kano, W. Denk, M. Häusser, Targeted patch-clamp recordings and single-cell electroporation of unlabeled neurons in vivo. *Nat. Methods* **5**, 61–67 (2008).
4. T. W. Margrie, A. H. Meyer, A. Caputi, H. Monyer, M. T. Hasan, A. T. Schaefer, W. Denk, M. Brecht, Targeted whole-cell recordings in the mammalian brain in vivo. *Neuron* **39**, 911–918 (2003).
5. D. Ishikawa, N. Takahashi, T. Sasaki, A. Usami, N. Matsuki, Y. Ikegaya, Fluorescent pipettes for optically targeted patch-clamp recordings. *Neural Netw.* **23**, 669–672 (2010).
6. T. Sasaki, N. Matsuki, Y. Ikegaya, Targeted axon-attached recording with fluorescent patch-clamp pipettes in brain slices. *Nat. Protoc.* **7**, 1228–1234 (2012).
7. B. K. Andrásfalvy, G. L. Galiñanes, D. Huber, M. Barbic, J. J. Macklin, K. Susumu, J. B. Delehanty, A. L. Huston, J. K. Makara, I. L. Medintz, Quantum dot-based multiphoton fluorescent pipettes for targeted neuronal electrophysiology. *Nat. Methods* **11**, 1237–1241 (2014).
8. K. Jayant, J. J. Hirtz, I. J.-L. Plante, D. M. Tsai, W. D. A. M. De Boer, A. Semonche, D. S. Peterka, J. S. Owen, O. Sahin, K. L. Shepard, R. Yuste, Targeted intracellular voltage recordings from dendritic spines using quantum-dot-coated nanopipettes. *Nat. Nanotechnol.* **12**, 335–342 (2017).
9. K. Jayant, M. Wenzel, Y. Bando, J. P. Hamm, N. Mandriota, J. H. Rabinowitz, I. J.-L. Plante, J. S. Owen, O. Sahin, K. L. Shepard, R. Yuste, Flexible nanopipettes for minimally invasive intracellular electrophysiology in vivo. *Cell Rep.* **26**, 266–278.e5 (2019).
10. H. Ow, D. R. Larson, M. Srivastava, B. A. Baird, W. W. Webb, U. Wiesner, Bright and stable core-shell fluorescent silica nanoparticles. *Nano Lett.* **5**, 113–117 (2005).
11. E. Neher, Ion channels for communication between and within cells. *Science* **256**, 498–502 (1992).
12. J. Becquerel, H. K. Onnes, in *Proceedings of the Royal Netherlands Academy of Arts and Sciences* (KNAW, 1908), vol. 10, pp. 1907–1908.
13. H. A. Bethe, Splitting of terms in crystals. *Ann. Physik* **3**, 133 (1929).
14. W. Carnall, P. Fields, K. Rajnak, Electronic energy levels of the trivalent lanthanide aquo ions. III. Tb^{3+}. *J. Chem. Phys.* **49**, 4447–4449 (1968).
15. R. Reisfeld, E. Greenberg, R. Velapoldi, B. Barnett, Luminescence quantum efficiency of Gd and Tb in borate glasses and the mechanism of energy transfer between them. *J. Chem. Phys.* **56**, 1698–1705 (1972).
16. T. Yamashita, Y. Ohishi, Concentration and temperature effects on the spectroscopic properties of Tb^{3+} doped borosilicate glasses. *J. Appl. Phys.* **102**, 123107 (2007).
17. P. Yasaka, J. Kaewkhao, in *2015 4th International Conference on Instrumentation, Communications, Information Technology, and Biomedical Engineering (ICICI-BME)* (IEEE, 2015), pp. 4–15.
18. G. H. Dieke, H. M. Crosswhite, B. Dunn, Emission spectra of the doubly and triply ionized rare earths. *JOSA* **51**, 820–827 (1961).
19. M. L. Bieber, V. J. Volbrecht, J. S. Werner, Spectral efficiency measured by heterochromatic flicker photometry is similar in human infants and adults. *Vision Res.* **35**, 1385–1392 (1995).
20. R. M. Boynton, History and current status of a physiologically based system of photometry and colorimetry. *J. Opt. Soc. Am. A Opt. Image Sci. Vis.* **13**, 1609–1621 (1996).
21. C. R. Cadwell, A. Palasantza, X. Jiang, P. Berens, Q. Deng, M. Yilmaz, J. Reimer, S. Shen, M. Bethge, K. F. Tolias, R. Sandberg, A. S. Tolias, Electrophysiological, transcriptomic and morphologic profiling of single neurons using Patch-seq. *Nat. Biotechnol.* **34**, 199–203 (2016).
22. C. R. Cadwell, F. Scala, P. G. Fahey, D. Kobak, S. Mulherkar, F. H. Sinz, S. Papadopoulos, Z. H. Tan, P. Johnsson, L. Hartmanis, S. Li, R. J. Cotton, K. F. Tolias, R. Sandberg, P. Berens, X. Jiang, A. S. Tolias, Cell type composition and circuit organization of clonally related excitatory neurons in the juvenile mouse neocortex. *eLife* **9**, e52951 (2020).
23. J. Fuzik, A. Zeisel, Z. Máté, D. Calvigioni, Y. Yanagawa, G. Szabó, S. Linnarsson, T. Harkany, Integration of electrophysiological recordings with single-cell RNA-seq data identifies neuronal subtypes. *Nat. Biotechnol.* **34**, 175–183 (2016).
24. H. Kameda, H. Hioki, Y. H. Tanaka, T. Tanaka, J. Sohn, T. Sonomura, T. Furuta, F. Fujiyama, T. Kaneko, Parvalbumin-producing cortical interneurons receive inhibitory inputs on proximal portions and cortical excitatory inputs on distal dendrites. *Eur. J. Neurosci.* **35**, 838–854 (2012).
25. E. Neher, B. Sakmann, Single-channel currents recorded from membrane of denervated frog muscle fibres. *Nature* **260**, 799–802 (1976).
26. R. Furman, J. C. Tanaka, Patch electrode glass composition affects ion channel currents. *Biophys. J.* **53**, 287–292 (1988).
27. C. Zuazaga, A. Steinacker, Patch-clamp recording of ion channels: iNterfering effects of patch pipette glass. *Phys. Ther.* **5**, 155–158 (1990).
28. N. Fertig, R. H. Blick, J. C. Behrends, Whole cell patch clamp recording performed on a planar glass chip. *Biophys. J.* **82**, 3056–3062 (2002).
29. M. Schieder, K. Rötzer, A. Brüggemann, M. Biel, C. Wahl-Schott, Planar patch clamp approach to characterize ionic currents from intact lysosomes. *Sci. Signal.* **3**, pl3 (2010).
30. I. Kolb, W. A. Stoy, E. B. Rousseau, O. A. Moody, A. Jenkins, C. R. Forest, Cleaning patch-clamp pipettes for immediate reuse. *Sci. Rep.* **6**, 35001 (2016).
31. S. B. Kodandaramaiah, G. T. Franzesi, B. Y. Chow, E. S. Boyden, C. R. Forest, Automated whole-cell patch-clamp electrophysiology of neurons in vivo. *Nat. Methods* **9**, 585–587 (2012).
32. S. B. Kodandaramaiah, G. L. Holst, I. R. Wickersham, A. C. Singer, G. T. Franzesi, M. L. McKinnon, C. R. Forest, E. S. Boyden, Assembly and operation of the autopatcher for automated intracellular neural recording in vivo. *Nat. Protoc.* **11**, 634–654 (2016).
33. Y. Peng, F. X. Mittermaier, H. Planert, U. C. Schneider, H. Alle, J. R. P. Geiger, High-throughput microcircuit analysis of individual human brains through next-generation multineuron patch-clamp. *eLife* **8**, e48178 (2019).
34. H. J. Suk, I. van Welie, S. B. Kodandaramaiah, B. Allen, C. R. Forest, E. S. Boyden, Closed-loop real-time imaging enables fully automated cell-targeted patch-clamp neural recording in vivo. *Neuron* **96**, 244–245 (2017).
35. L. A. Annecchino, A. R. Morris, C. S. Copeland, O. E. Agabi, P. Chadderton, S. R. Schultz, Robotic automation of in vivo two-photon targeted whole-cell patch-clamp electrophysiology. *Neuron* **95**, 1048–1055.e3 (2017).
36. G. E. Peterson, P. M. Bridenbaugh, Fluorescent lifetime of terbium in the presence of other rare-earth ions. *JOSA* **53**, 301–302 (1963).
37. G. Aka, A. Kahn-Harari, F. Mougel, D. Vivien, F. Salin, P. Coquelin, P. Colin, D. Pelenc, J. P. Damelet, Linear- and nonlinear-optical properties of a new gadolinium calcium oxoborate crystal, $Ca_4GdO(BO_3)_3$. *JOSA B* **14**, 2238–2247 (1997).
38. P. Wang, J. M. Dawes, P. Dekker, D. S. Knowles, J. A. Piper, B. Lu, Growth and evaluation of ytterbium-doped yttrium aluminum borate as a potential self-doubling laser crystal. *JOSA B* **16**, 63–69 (1999).
39. G.-L. Law, K.-L. Wong, C. W.-Y. Man, W.-T. Wong, S.-W. Tsao, M. H.-W. Lam, P. K.-S. Lam, Emissive terbium probe for multiphoton in vitro cell imaging. *J. Am. Chem. Soc.* **130**, 3714–3715 (2008).

40. N. Rakov, W. Lozano, E. L. Falcão-Filho, R. B. Guimarães, G. S. Maciel, C. B. de Araújo, Three- and four-photon excited upconversion luminescence in terbium doped lutetium silicate powders by femtosecond laser irradiation. *Opt. Mater. Express* **3**, 1803–1809 (2013).
41. D. G. Ouzounov, T. Wang, M. Wang, D. D. Feng, N. G. Horton, J. C. Cruz-Hernández, Y. T. Cheng, J. Reimer, A. S. Tolias, N. Nishimura, C. Xu, In vivo three-photon imaging of activity of GCaMP6-labeled neurons deep in intact mouse brain. *Nat. Methods* **14**, 388–390 (2017).
42. T. Wang, D. G. Ouzounov, C. Wu, N. G. Horton, B. Zhang, C. H. Wu, Y. Zhang, M. J. Schnitzer, C. Xu, Three-photon imaging of mouse brain structure and function through the intact skull. *Nat. Methods* **15**, 789–792 (2018).
43. C. A. Lazar, I. Rau, A.-M. Manea, Fluorescence, optical absorption and third-order nonlinear optical properties of terbium (III) complex embedded into DNA-CTMA matrix. *JOL* **182**, 59–64 (2017).
44. D. Gloge, Weakly guiding fibers. *Appl. Optics* **10**, 2252–2258 (1971).
45. S. Chen, A. Z. Weitemier, X. Zeng, L. He, X. Wang, Y. Tao, A. J. Y. Huang, Y. Hashimotodani, M. Kano, H. Iwasaki, L. K. Parajuli, S. Okabe, D. B. L. Teh, A. H. All, I. Tsutsui-Kimura, K. F. Tanaka, X. Liu, T. J. McHugh, Near-infrared deep brain stimulation via upconversion nanoparticle-mediated optogenetics. *Science* **359**, 679–684 (2018).
46. M. S. Patterson, B. C. Wilson, D. R. Wyman, The propagation of optical radiation in tissue I. Models of radiation transport and their application. *Lasers Med. Sci.* **6**, 155–168 (1991).
47. M. Metlay, The fluorescence of the europium and terbium dibenzoylmethides. *J. Electrochem. Soc.* **111**, 1253 (1964).
48. R. Reisfeld, E. Greenberg, R. N. Brown, M. G. Drexhage, C. K. Jørgensen, Fluorescence of europium (III) in a flouride glass containing zirconium. *Chemical Physics Letters* **95**, 91–94 (1983).
49. K. Matsui, C. E. Jahr, M. E. Rubio, High-concentration rapid transients of glutamate mediate neural-glial communication via ectopic release. *J. Neurosci.* **25**, 7538–7547 (2005).
50. R. Nakano, N. Ihara, S. Morikawa, A. Nakashima, M. T. Kanemaki, Y. Ikegaya, H. Takeuchi, Auxin-mediated rapid degradation of target proteins in hippocampal neurons. *Neuroreport* **30**, 908–913 (2019).
51. K. Okamoto, N. Hitora-Imamura, H. Hioki, Y. Ikegaya, GABAergic malfunction in the anterior cingulate cortex underlying maternal immune activation-induced social deficits. *J. Neuroimmunol.* **321**, 92–96 (2018).
52. R. Koyama, R. Muramatsu, T. Sasaki, R. Kimura, C. Ueyama, M. Tamura, N. Tamura, J. Ichikawa, N. Takahashi, A. Usami, M. K. Yamada, N. Matsuki, Y. Ikegaya, A low-cost method for brain slice cultures. *J. Pharmacol. Sci.* **104**, 191–194 (2007).
53. T. Sasaki, N. Matsuki, Y. Ikegaya, Action-potential modulation during axonal conduction. *Science* **331**, 599–601 (2011).
54. Y. Yamagata, S. Kobayashi, T. Umeda, A. Inoue, H. Sakagami, M. Fukaya, M. Watanabe, N. Hatanaka, M. Totsuka, T. Yagi, K. Obata, K. Imoto, Y. Yanagawa, T. Manabe, S. Okabe, Kinase-dead knock-in mouse reveals an essential role of kinase activity of Ca^{2+}/calmodulin-dependent protein kinase IIalpha in dendritic spine enlargement, long-term potentiation, and learning. *J. Neurosci.* **29**, 7607–7618 (2009).
55. Y. Masamizu, Y. R. Tanaka, Y. H. Tanaka, R. Hira, F. Ohkubo, K. Kitamura, Y. Isomura, T. Okada, M. Matsuzaki, Two distinct layer-specific dynamics of cortical ensembles during learning of a motor task. *Nat. Neurosci.* **17**, 987–994 (2014).
56. M. Kondo, K. Kobayashi, M. Ohkura, J. Nakai, M. Matsuzaki, Two-photon calcium imaging of the medial prefrontal cortex and hippocampus without cortical invasion. *eLife* **6**, (2017).
57. J.-H. Jean, C.-R. Chang, R.-L. Chang, T.-H. Kuan, Effect of alumina particle size on prevention of crystal growth in low-k silica dielectric composite. *Mater. Chem. Phys.* **40**, 50–55 (1995).

Acknowledgments: We thank K. Matsui for advice on the electrophysiological method. We thank the members of the Laboratory of Morphology and Image Analysis, Research Support Center, Juntendo University Graduate School of Medicine for technical assistance with scanning electron microscopy. **Funding:** This work was supported by JST ERATO (JPMJER1801), JSPS Grants-in-Aid for Scientific Research (18H05525; 19H05307), the Center of Innovation Program funded by the Japan Science and Technology Agency, and the Human Frontier Science Program (RGP0019/2016). This research was partially supported by the Institute of AI and Beyond of The University of Tokyo. This work was conducted partially as a program at the International Research Center for Neurointelligence (WPI-IRCN) of The University of Tokyo Institutes for Advanced Study at The University of Tokyo. **Author contributions:** K.O. and Y.I. designed and implemented the study and wrote the manuscript. K.O., T.K., R.N., and H.T. performed in vitro physiology and optical recording experiments. T.E., Y.S., and M.M. performed in vivo physiology and optical recording experiments. N.F. developed the glass capillaries. K.K. and J.Y. helped perform THG measurements. H.H. performed image acquisition. All authors discussed the results and commented on the manuscript. **Competing interests:** The authors declare that they have no competing interests. **Data and materials availability:** All data needed to evaluate the conclusions in the paper are present in the paper and/or the Supplementary Materials. Additional data related to this paper may be requested from the authors.

Submitted 10 June 2020
Accepted 12 November 2020
Published 6 January 2021
10.1126/sciadv.abd2529

Citation: K. Okamoto, T. Ebina, N. Fujii, K. Konishi, Y. Sato, T. Kashima, R. Nakano, H. Hioki, H. Takeuchi, J. Yumoto, M. Matsuzaki, Y. Ikegaya, Tb^{3+}-doped fluorescent glass for biology. *Sci. Adv.* **7**, eabd2529 (2021).